Published in "Journal of Physics B: Atomic, Molecular and Optical Physics
42 (4): 044009, 2009" which should be cited to refer to this work.

# Absolute angle-differential cross sections for electron-impact excitation of neon within the first 3.5 eV above threshold

**M Allan[1], K Franz[1,2], H Hotop[2], O Zatsarinny[3] and K Bartschat[3]**

[1] Département de Chimie, Université de Fribourg, Fribourg, Suisse, Switzerland
[2] Fachbereich Physik, Technische Universität Kaiserslautern, 67653 Kaiserslautern, Germany
[3] Department of Physics and Astronomy, Drake University, Des Moines, IA 50311, USA



**Abstract**

Absolute angle-differential cross sections for excitation of neon atoms to the four $2p^5 3s$ and to selected $2p^5 3p$ levels have been determined as a function of electron energy up to 3.5 eV above threshold at the scattering angles of 0°, 45°, 90°, 135° and 180°. In addition, the cross sections were recorded as function of scattering angle from 0° to 180° at 18 eV for the $2p^5 3s$ levels and at 19.3 eV for the $2p^5 3p$ levels, respectively. The cross sections were also determined theoretically using the Breit–Pauli *B*-spline *R*-matrix method with non-orthogonal orbital sets. Very good agreement is found both in terms of absolute values and in terms of the energies and widths of the numerous resonant features, thereby allowing for (re)classifications with significantly improved accuracy compared to earlier work.

## 1. Introduction

Absolute cross sections for inelastic electron scattering from rare-gas atoms are of great importance for gaseous discharge physics [1], but—except for helium—the theoretical description of these processes has remained a substantial challenge. Recently, however, significant progress has been made by means of a *B*-spline *R*-matrix method [2–4]. The key feature of this method is the possibility of using *non-orthogonal* sets of term-dependent one-electron orbitals. This allows for an accurate target description with relatively small configuration expansions. Excellent agreement was observed, for instance, between the calculated energy-dependent cross sections for the production of metastable Ne [2] and Ar [3] atoms with those measured in high-resolution experiments [5–7]. For Ne, a very sharp resonance (energy 18.527 meV, width 0.8 meV) was theoretically predicted [2] and subsequently confirmed experimentally [7].

For thorough tests of theoretical approaches, it is highly desirable to compare the computed results with detailed experimental information, such as angle-differential excitation cross sections, obtained in absolute units at energies *near threshold,* where the excitation process is dominated by prominent resonance structure [5]. A particular point of interest is the final-state-specific coupling of the anion resonances. Apart from numerous work on He (see, e.g., [5, 8–10] and some results for Ne [5–7], Ar [5, 6] and Kr [5, 11]), such data are currently missing in the literature.

Here we report on absolute angle-differential cross sections for excitation of neon atoms to the four levels of the $2p^5 3s$ configuration and to selected levels of the $2p^5 3p$ configuration in the near-threshold energy range up to 3.5 eV above threshold. Most of the prominent anion resonances for incident energies below 19 eV have been resolved previously [2, 5–7]. Earlier angle-differential work on Ne ($2p^5 3s$) excitation was carried out at a few discrete impact energies $\geqslant$20 eV. The two studies, which include measurements at 20 eV and therefore overlap with the present energy range, are those of Register *et al* [12] and Khakoo *et al* [13]. A small subset of our data for Ne ($2p^5 3s$) excitation was presented in a recent letter [14]. The present paper extends the experimental results to more scattering angles, higher energies, and also presents angular distributions. Moreover, it includes results for selected levels of the $2p^5 3p$ configuration.

The theoretical method has also been improved by including even more accurate target wavefunctions. While the earlier work [2, 7] used the same set of correlated orbitals for all states, these orbitals were now optimized for each term

separately. Furthermore, the close-coupling expansion was extended by including the $2p^54p$ and $2p^55s$ levels, thereby resulting in 14 additional target states.

This paper is organized as follows. After a brief summary of the experimental method and the extensions of the theoretical model compared to the previous calculations, we present and compare our results for the $2p^53s$ and $2p^53p$ levels. This is followed by a detailed analysis of the resonance features, particularly in the incident energy range of 18.9–20.2 eV, which is dominated by resonances.

## 2. Experiment

The experimental results were obtained with a high-resolution electron scattering apparatus [9] involving two-stage hemispherical analysers. The incident beam possesses an energy width (FWHM) of 10 meV. The energy-loss peaks have a width of 14 meV, thus permitting the resolution of all four Ne ($2p^53s$) levels and the majority of the Ne ($2p^53p$) levels. The present paper reports cross sections recorded as a function of electron energy at the scattering angles of 0°, 45°, 90°, 135° and 180°. The angles of 0° and 180° were reached with a magnetic angle changer [15] of special design [16]. The raw signal was corrected for the variations of the instrumental response with energy and scattering angle as described in [17].

The absolute inelastic values were determined in two steps. First, the values of the absolute elastic cross sections of neon were determined at 18.0, 19.3 and 20.0 eV by normalizing to helium [18] using the relative flow method [19]. They are reliable within about ±15%. Electron energy-loss spectra including both the elastic and the inelastic peaks were then recorded at constant incident energies of 18.0, 19.3 and 20.0 eV and corrected for the analyser response function. Absolute inelastic values were determined from the elastic and inelastic signal intensities in the energy loss by normalizing to the absolute elastic values determined in the first step. This procedure was carried out at each of the scattering angles 0°, 45°, 90°, 135° and 180°. The energy-loss spectra cover a large span of scattered electron energies, and hence accurate knowledge of the response function over this energy range is critical for the determination of accurate values of the inelastic cross sections. The uncertainty of the response function makes the errors of the absolute inelastic cross sections larger than that of the elastic cross section. They become about ±20% for energies more than 0.3 eV above each threshold. At lower energies, the response function becomes even more difficult to determine and the error bars increase gradually, reaching ±50% very near threshold.

The energy-loss spectrum in figure 1 displays the low-lying electronic levels of neon and illustrates the experimental conditions used in the present work. The $2p^53s$ levels are fully resolved, while partial overlap occurs among some of the $2p^53p$ levels. In these cases, Gaussian fits were used to obtain the areas under the peaks.

The angular distributions were measured in three overlapping sections, by sweeping the magnetic angle changer over a ±45° range around each of the mechanically given centre angles 45, 90, 135° and piecing the results together.

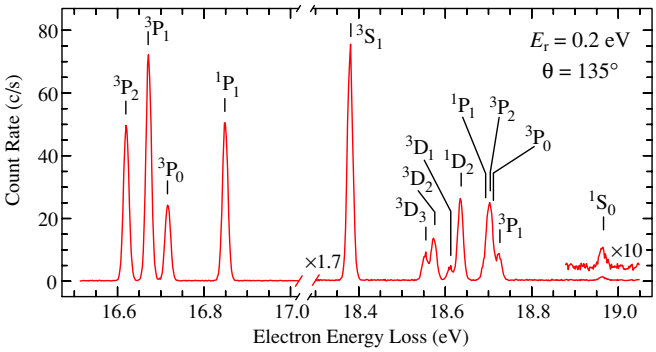


**Figure 1.** Electron energy-loss spectrum of Ne taken at 135° with a fixed residual electron energy of 0.2 eV.

Each section was corrected for the instrumental response function determined on elastic scattering in helium and normalized to the absolute values determined above.

## 3. Theory

The numerical calculations performed for the present work are based upon the semi-relativistic *B*-spline *R*-matrix (BSR) approach described in [2, 3, 20]. Details of this particular method and references to earlier work can be found in these papers. As mentioned above, the key feature of this approach is to significantly improve the target description by using compact configuration–interaction expansions involving non-orthogonal sets of term-dependent one-electron orbitals.

Despite the accuracy achieved previously [2, 3, 14], the theoretical model had to be further improved for the present work in order to extend the energy range for which resonances could be analysed in detail, to obtain accurate results for the $2p^53p$ levels, and to enlarge the overall energy region to 22 eV. Specifically, we optimized the correlation orbitals for each term separately, and we extended the close-coupling expansion to also include the physical $2p^54p$ and $2p^55s$ levels. This resulted in a 45-state BSR calculation, with up to 169 coupled channels.

The description of the scattering wavefunction for a given partial wave contained up to 40 000 configurations and up to 420 different non-orthogonal one-electron orbitals. The *R*-matrix radius was chosen as $50a_0$, with $a_0 = 0.529 \times 10^{-10}$ m denoting the Bohr radius. We employed 79 *B*-splines of order 8 for each one-electron radial function. This resulted in interaction matrices with dimensions up to 13 600 to be diagonalized for each partial wave.

Table 1 shows the absolute energies of the 45 physical target states included in our calculation, together with the experimental excitation energies relative to the ground state and the difference between experimental and theoretical binding energies. As described previously [2], the states were generated with the *B*-spline box-based close-coupling method [22], except for the separate optimization of the correlation orbitals and the use of physical 4p and 5s orbitals for the

**Table 1.** Calculated and observed [21] excitation energies for the lowest 45 states of neon. The last column presents the differences between the experimental and theoretical ionization potentials. For the lowest 15 states, we present both the pair-coupling and the $LS$-classification.

| State | Theory (au) | Expt. (eV) | Diff. (eV) |
|---|---|---|---|
| $(2p^6)^1S_0$ | −128.744 051 11 | 0 | 0.041 |
| $3s[3/2]_2(^3P_2)$ | −128.132 117 39 | 16.619 | 0.009 |
| $3s[3/2]_1(^3P_1)$ | −128.130 110 47 | 16.671 | 0.006 |
| $3s'[1/2]_0(^3P_0)$ | −128.128 415 29 | 16.715 | 0.004 |
| $3s'[1/2]_1(^1P_1)$ | −128.123 049 54 | 16.848 | −0.009 |
| $3p[1/2]_1(^3S_1)$ | −128.067 005 01 | 18.382 | −0.000 |
| $3p[5/2]_3(^3D_3)$ | −128.060 707 39 | 18.555 | 0.002 |
| $3p[5/2]_2(^3D_2)$ | −128.059 945 89 | 18.576 | 0.002 |
| $3p[3/2]_1(^3D_1)$ | −128.058 563 67 | 18.613 | 0.001 |
| $3p[3/2]_2(^1D_2)$ | −128.057 729 21 | 18.637 | 0.002 |
| $3p'[3/2]_1(^1P_1)$ | −128.055 564 41 | 18.693 | −0.000 |
| $3p'[3/2]_2(^3P_2)$ | −128.055 110 77 | 18.704 | −0.002 |
| $3p[3/2]_0(^3P_0)$ | −128.054 801 06 | 18.711 | −0.003 |
| $3p'[1/2]_1(^3P_1)$ | −128.054 308 14 | 18.726 | −0.001 |
| $3p'[1/2]_0(^1S_0)$ | −128.044 046 36 | 18.966 | −0.041 |
| $4s[3/2]_2$ | −128.019 918 55 | 19.664 | 0.001 |
| $4s[3/2]_1$ | −128.018 987 42 | 19.688 | −0.000 |
| $4s'[1/2]_0$ | −128.016 215 30 | 19.761 | −0.003 |
| $4s'[1/2]_1$ | −128.015 474 36 | 19.780 | −0.004 |
| $3d[1/2]_0$ | −128.006 355 19 | 20.025 | −0.008 |
| $3d[1/2]_1$ | −128.006 313 58 | 20.026 | −0.007 |
| $3d[7/2]_4$ | −128.006 200 30 | 20.035 | −0.002 |
| $3d[7/2]_3$ | −128.006 179 29 | 20.035 | −0.002 |
| $3d[3/2]_2$ | −128.005 991 90 | 20.037 | −0.006 |
| $3d[3/2]_1$ | −128.005 923 14 | 20.040 | −0.004 |
| $3d[5/2]_2$ | −128.005 709 17 | 20.048 | −0.002 |
| $3d[5/2]_3$ | −128.005 699 93 | 20.048 | −0.002 |
| $3d'[5/2]_1$ | −128.002 320 76 | 20.136 | −0.006 |
| $3d'[5/2]_3$ | −128.002 305 98 | 20.136 | −0.006 |
| $3d'[3/2]_2$ | −128.002 192 56 | 20.138 | −0.008 |
| $3d'[3/2]_1$ | −128.002 150 91 | 20.139 | −0.007 |
| $4p[1/2]_1$ | −128.002 076 95 | 20.150 | 0.001 |
| $4p[5/2]_3$ | −128.000 636 10 | 20.188 | 0.000 |
| $4p[5/2]_2$ | −128.000 310 22 | 20.197 | 0.000 |
| $4p[3/2]_1$ | −127.999 881 15 | 20.211 | 0.002 |
| $4p[3/2]_2$ | −127.999 670 49 | 20.214 | −0.000 |
| $4p[3/2]_0$ | −127.997 871 71 | 20.259 | −0.004 |
| $4p'[3/2]_1$ | −127.996 754 79 | 20.291 | −0.003 |
| $4p'[3/2]_2$ | −127.996 529 77 | 20.297 | −0.003 |
| $4p'[1/2]_1$ | −127.996 468 22 | 20.297 | −0.004 |
| $4p'[1/2]_0$ | −127.993 451 85 | 20.369 | −0.015 |
| $5s[3/2]_2$ | −127.986 967 72 | 20.560 | 0.000 |
| $5s[3/2]_1$ | −127.986 561 20 | 20.571 | −0.000 |
| $5s'[1/2]_0$ | −127.983 268 39 | 20.657 | −0.004 |
| $5s'[1/2]_1$ | −127.983 026 59 | 20.663 | −0.004 |

additional target states mentioned above. This is the reason for the small differences in the energies of the lowest 31 states compared to those given before.

Finally, we used the program MJK of Grum-Grzhimailo [23] to calculate the differential cross sections from the $\boldsymbol{T}$-matrix elements produced by the asymptotic program FARM [24]. Contributions up to a total electronic angular momentum $J = 25/2$ of the projectile−target collision system were sufficient to converge the partial-wave expansion for all transitions and energies of interest.

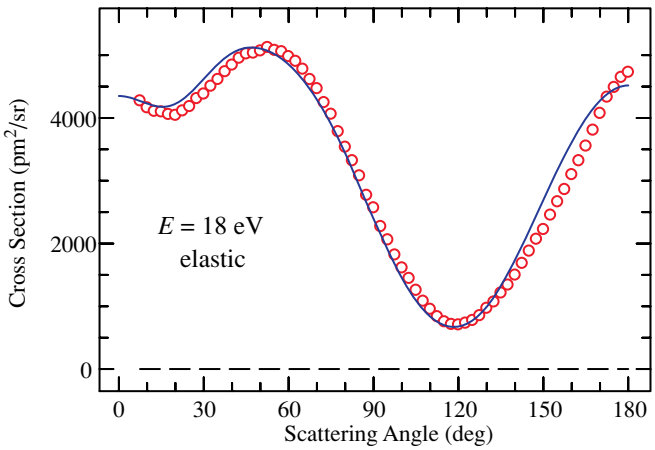


**Figure 2.** Angle-differential cross section for elastic e–Ne scattering at an incident electron energy of 18 eV. The experimental data are indicated by circles and the theoretical predictions by the full curve.

## 4. Results and discussion

As a first test, we compare in figure 2 experimental data and theoretical predictions for the angle-differential elastic cross section for electron scattering from neon atoms in their ground state at an incident energy of 18.0 eV. The excellent agreement provides some confidence in the results for the inelastic transitions to be presented below.

We begin with excitation of the $2p^5 3s$ states (subsection 4.1) and selected members of the $2p^5 3p$ manifold (subsection 4.2). This is followed by a detailed analysis of the resonance structure in subsection 4.3.

### *4.1. Excitation of the $2p^5 3s$ states*

In figures 3–7 we compare the experimental cross section for the excitation of the four $2p^5 3s$ states, obtained at the scattering angles of 0°, 45°, 90°, 135° and 180° with the corresponding predictions from the $B$-spline $R$-matrix approach. Recall that the absolute magnitudes of the experimental results were determined independently of the current theory.

Before discussing the details, we also note that the theoretical results presented here are very similar, though not identical, to those reported in our earlier letter [14] for energies up to 19.3 eV. The minor changes in this energy region are due to the further improved numerical model described above. The extension of the model, however, was absolutely essential to reproduce the resonance structure in the incident range 19–20 eV discussed further below, as well as to obtain accurate results for the $2p^5 3p$ excitation functions at all energies.

Figures 3–7 demonstrate that theory and experiment generally agree within about 10% at energies more than 0.3 eV above threshold, well within the experimental error limit. The difference becomes larger closer to threshold, where the theoretical values are below experiment by 25% at 16.9 eV and by 40% at 16.7 eV. As pointed out earlier [14], these differences may be due to the difficulty of determining the response function for an inelastic process on the elastic scattering in helium. No contradiction between theory and experiment is

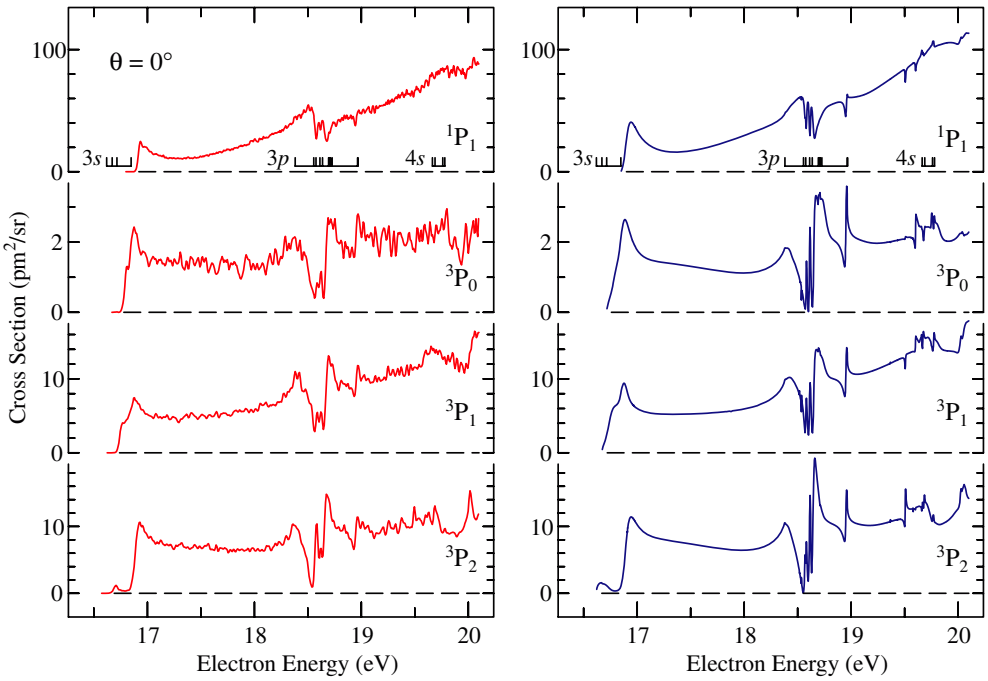


**Figure 3.** Absolute cross sections for excitation of the Ne ($2p^5 3s$) states at $\theta = 0°$. The experimental data are in the left and the theoretical predictions in the right panel. Thresholds for the 3s, 3p and 4s excitations are indicated below the top spectra.

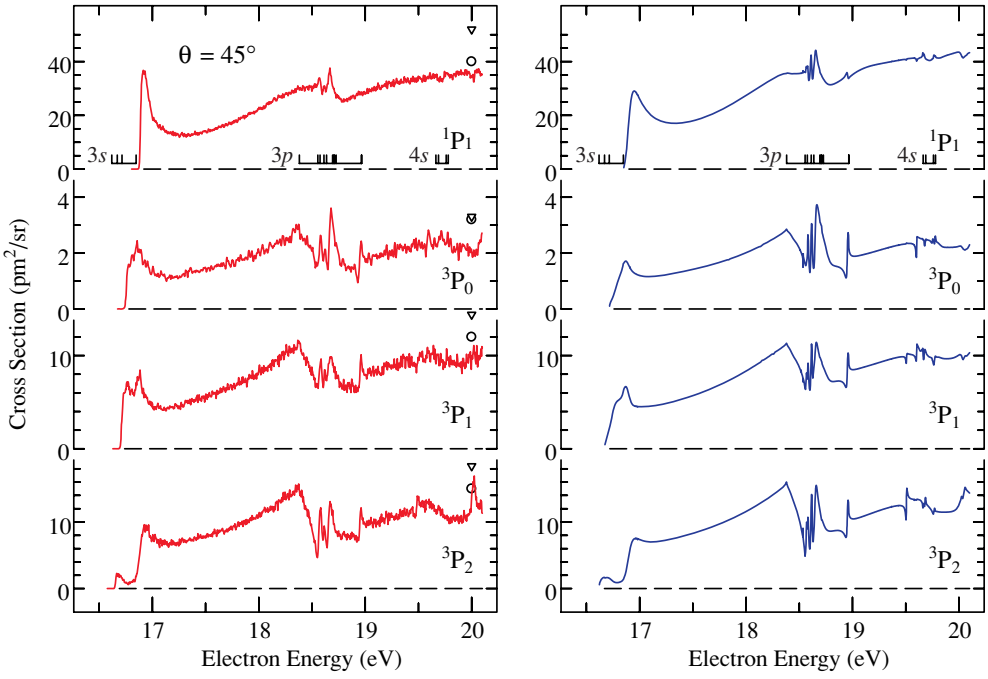


**Figure 4.** As figure 3 at $\theta = 45°$. The circles at 20 eV indicate the values of Register *et al* [12] and the triangles the data of Khakoo *et al* [13].

thus found over the entire energy range. The 20 eV data of Register *et al* [12] and of Khakoo *et al* [13] are indicated in the figures where appropriate. The agreement is generally within the combined error limits. Note that the comparison of the cross section magnitudes with the earlier single energy measurements at 20 eV is affected by the presence of a sharp resonance at 20.01 eV in several cases (see, for example, the bottom curve in figure 4). The earlier measurements at a single energy may thus depend on whether they were taken exactly at the resonance or slightly off. They also depend on resolution, which determines the width and height of the resonance peak.

Overall, theory and experiment agree remarkably well on the shapes, widths, and energies of the narrow resonant features in the 18.3–19.0 eV range of incident energies. Since these resonances are associated with the $2p^5 3p$ levels, they are even more prominent in most of the excitation functions shown in the following subsection.

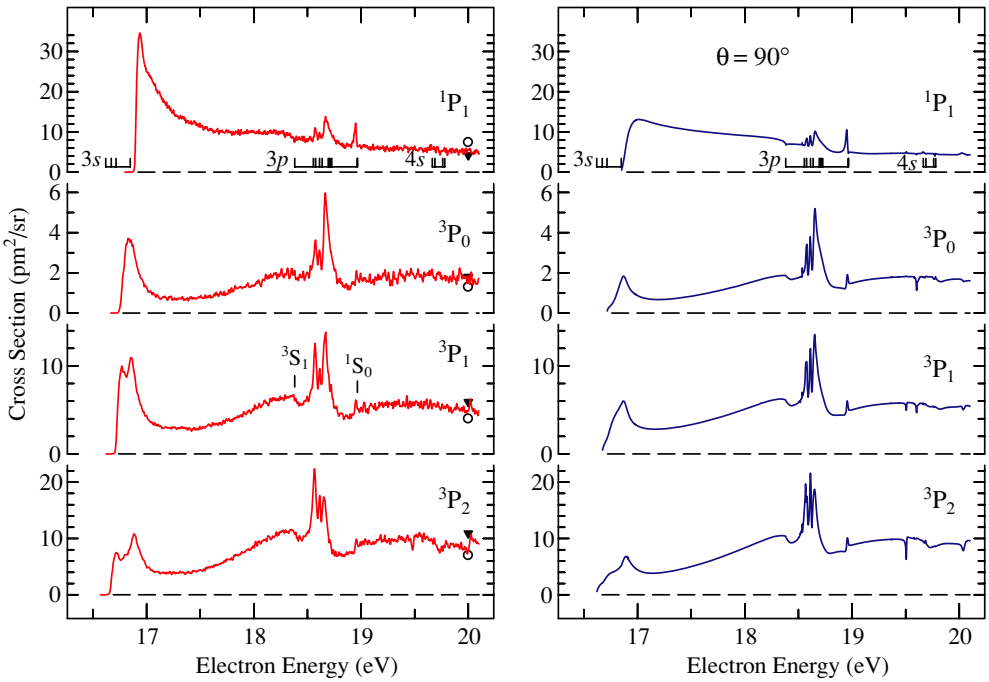


**Figure 5.** As figure 3 at $\theta = 90°$.

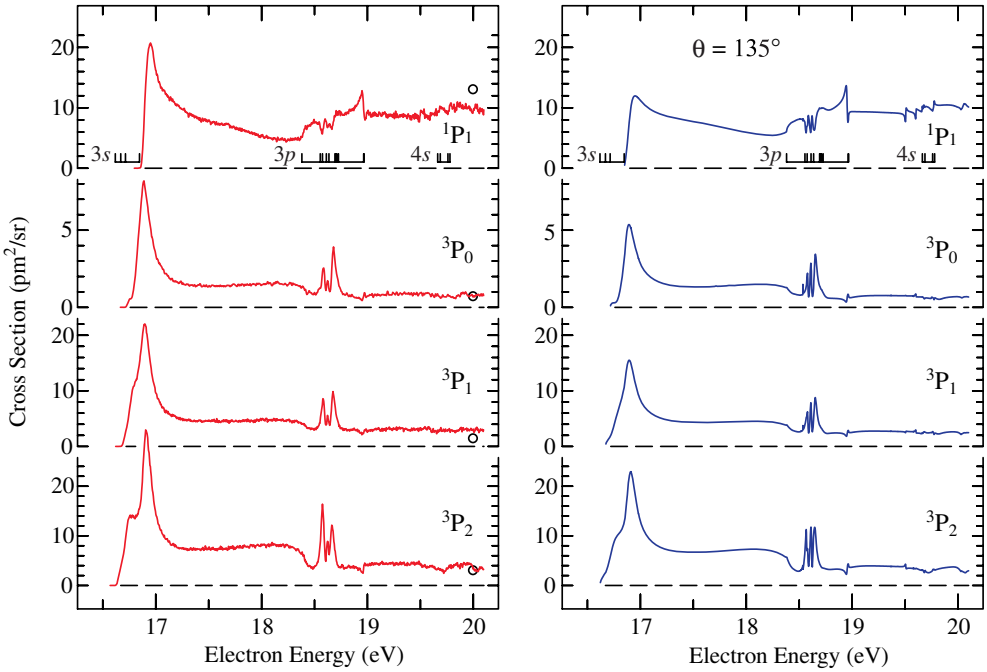


**Figure 6.** As figure 3 at $\theta = 135°$. The circles at 20 eV indicate the values of Register *et al* [12].

Figure 8 exhibits the angular distributions for excitation of the four states at the fixed incident energy of 18 eV. Very good agreement between experiment and theory is obtained for all states, except for as much as a 20% difference in the $^1P_1$ state cross section below 60°. Table 2 lists the integral and momentum-transfer cross sections derived from the experimental angular distributions and compares them to theoretical predictions. The agreement is very good for the elastic case and the 3s states. The results for the 3p states will be discussed in the following subsection.

### *4.2. Excitation of the $2p^5 3p$ states*

Figures 9–13 display the experimental and theoretical cross section for the excitation of four selected $2p^5 3p$ states, again obtained at the scattering angles of 0°, 45°, 90°, 135° and 180°, respectively. Note the strong dependence of the absolute values on the scattering angle. At 22 eV, for example, excitation of the $^1S_0$ state dominates for forward scattering (cf figure 9), while excitation of the $^3S_1$ state is most important for backward scattering angles (cf figure 13).

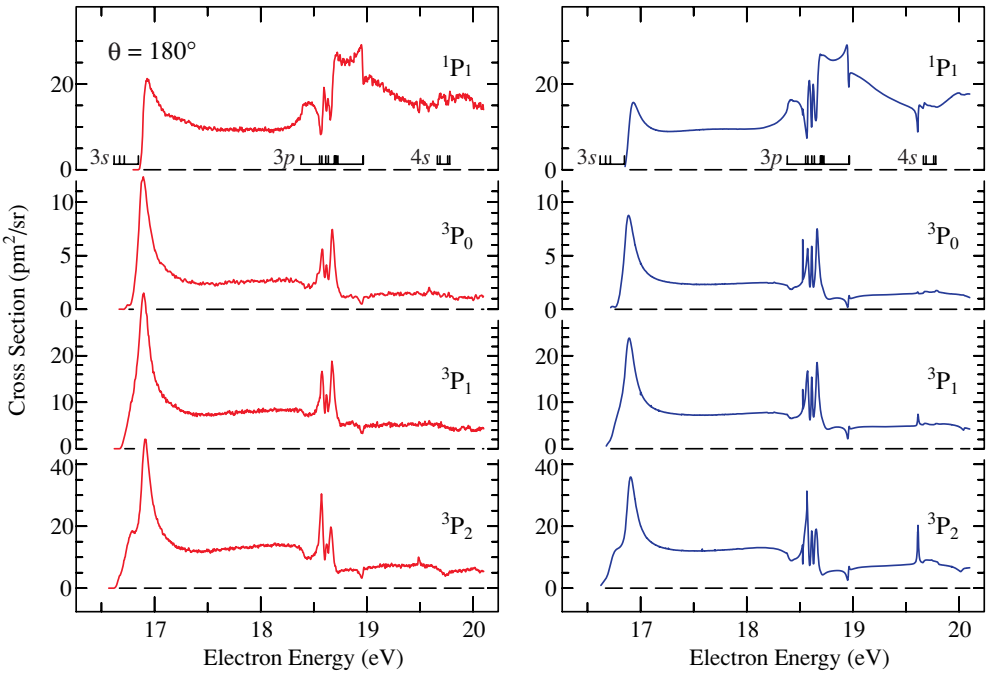


**Figure 7.** As figure 3 at $\theta = 180^\circ$.

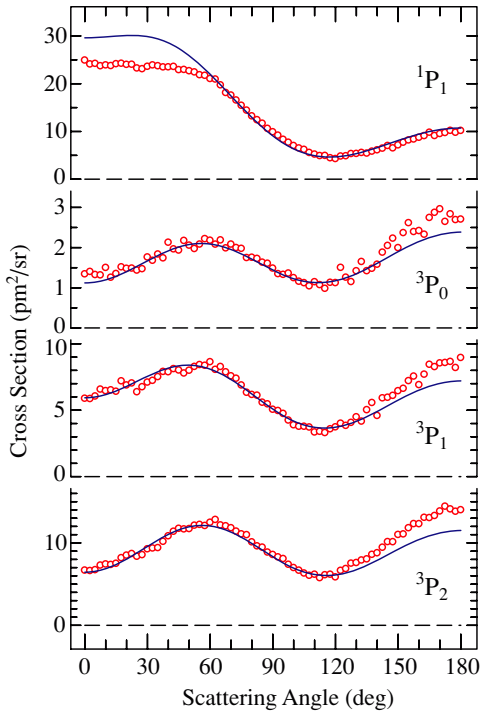


**Figure 8.** Cross sections for excitation of the Ne ($2p^5 3s$) states at an incident energy of $E = 18$ eV. The experimental data are indicated by circles and the theoretical predictions by lines.

Essentially all the features seen in the experiment below an incident electron energy of 20.2 eV are reproduced by the BSR theory, although some differences remain in the details. They include the steep rise of some excitation functions at 90°, which is less pronounced in the theory. This feature is also seen for the $2p^5 3s$ states and may at least partially be due to experimental difficulties. The overall agreement between experiment and theory is still very satisfactory, albeit not quite as good as for the ($2p^5 3s$) states. In some cases, the theoretical predictions exhibit wide maxima or minima in the region 20.5–22.0 eV, while the experimental energy dependence is close to linear in this energy range.

**Table 2.** Elastic and inelastic integral and momentum-transfer cross sections (ICS and MTCS, respectively), derived from the angular distributions shown in figures 2, 8 and 14.

| | | ICS (pm$^2$) | | MTCS (pm$^2$) | |
|---|---|---|---|---|---|
| State | $E$ (eV) | Experiment | Theory | Experiment | Theory |
| Elastic | 18.0 | $3.70 \times 10^4$ | $3.82 \times 10^4$ | $2.79 \times 10^4$ | $2.88 \times 10^4$ |
| $^3$P$_2$ | 18.0 | 117 | 113 | 112 | 105 |
| $^3$P$_1$ | 18.0 | 75 | 74 | 68 | 66 |
| $^3$P$_0$ | 18.0 | 21 | 20 | 21 | 20 |
| $^1$P$_1$ | 18.0 | 161 | 174 | 113 | 116 |
| $^3$S$_1$ | 19.3 | 12 | 13 | 18 | 19 |
| $^3$D$_3$ | 19.3 | 17 | 14 | 20 | 16 |
| $^3$D$_2$ | 19.3 | 20 | 19 | 21 | 19 |
| $^1$D$_2$ | 19.3 | 37 | 33 | 39 | 34 |
| $^1$S$_0$ | 19.3 | 56 | 39 | 24 | 14 |

Figure 14 shows the angular distributions at a fixed incident energy of 19.3 eV. Once again, the overall agreement between experiment and theory is very satisfactory, with the largest differences (up to 20%) occurring for the $^1$S$_0$ state at angles below 90° and for the remaining states for angles larger than 120°. Table 2 lists the integral and momentum-transfer cross sections derived from the experimental angular distributions and compares them to theoretical predictions. The agreement is very good in most cases, except for the ($2p^5 3p$)$^1$S$_0$ state, where the theoretical value is substantially

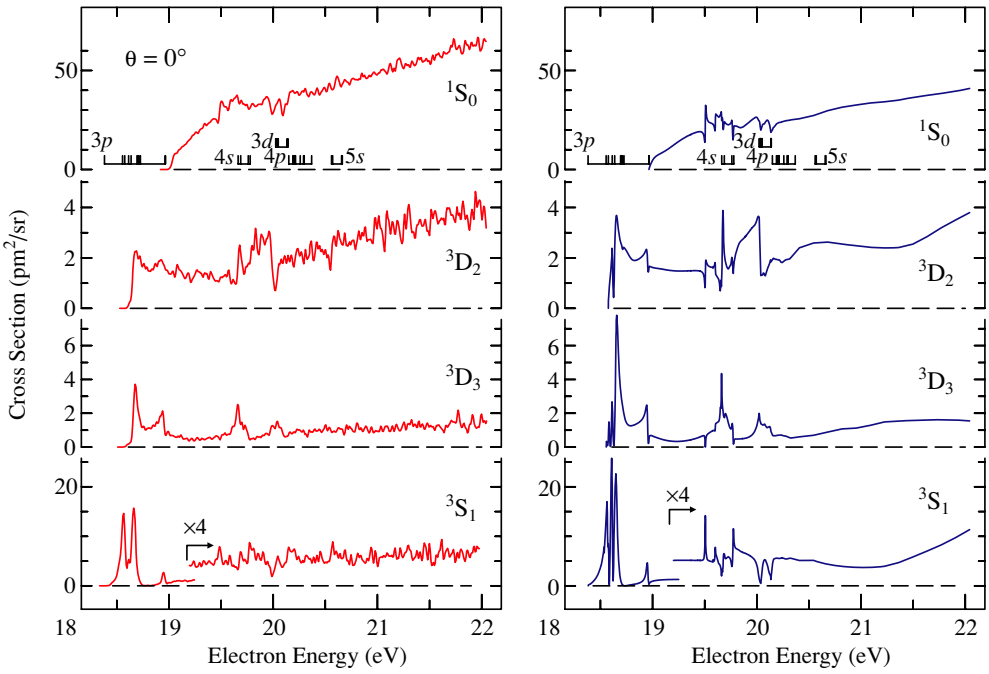


**Figure 9.** Absolute cross sections for excitation of the Ne ($2p^5 3p$) states at $\theta = 0°$. Note that the results for the $^3S_1$ state have been multiplied by 4 beyond 19.2 eV in order to improve the visibility. Thresholds are indicated below the top spectra.

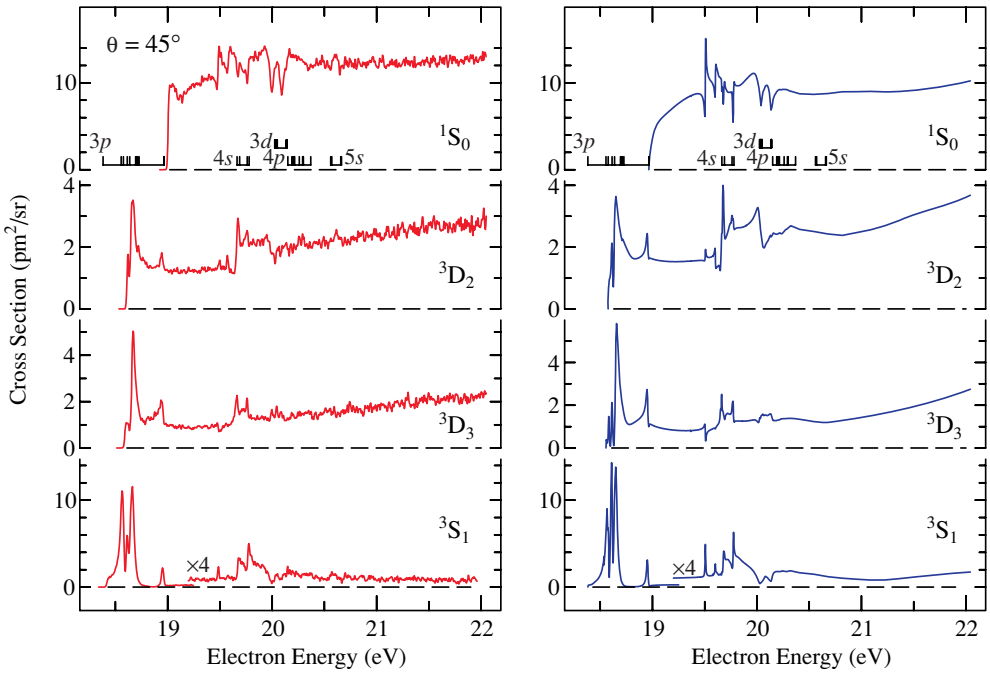


**Figure 10.** As figure 9 at $\theta = 45°$.

smaller than the experimental data. This is related to the fact that the cross section is strongly forward-peaked. The agreement of theory and experiment within about 20% in the forward direction is not unreasonable. However, the ICS and MTCS enhance the contributions in the central and even the backward part of the angular range. Here the cross section is very small and, although the absolute error is small, the relative error is comparatively large.

### *4.3. Classification of resonances*

As seen in the previous subsections, theory and experiment agree remarkably well on the shapes, widths and energies of the narrow resonance features seen in the various excitation functions between the respective thresholds and incident electron energies just above 20 eV, with the last matching feature seen around 20.2 eV. Although the close-coupling expansion in the current calculation includes

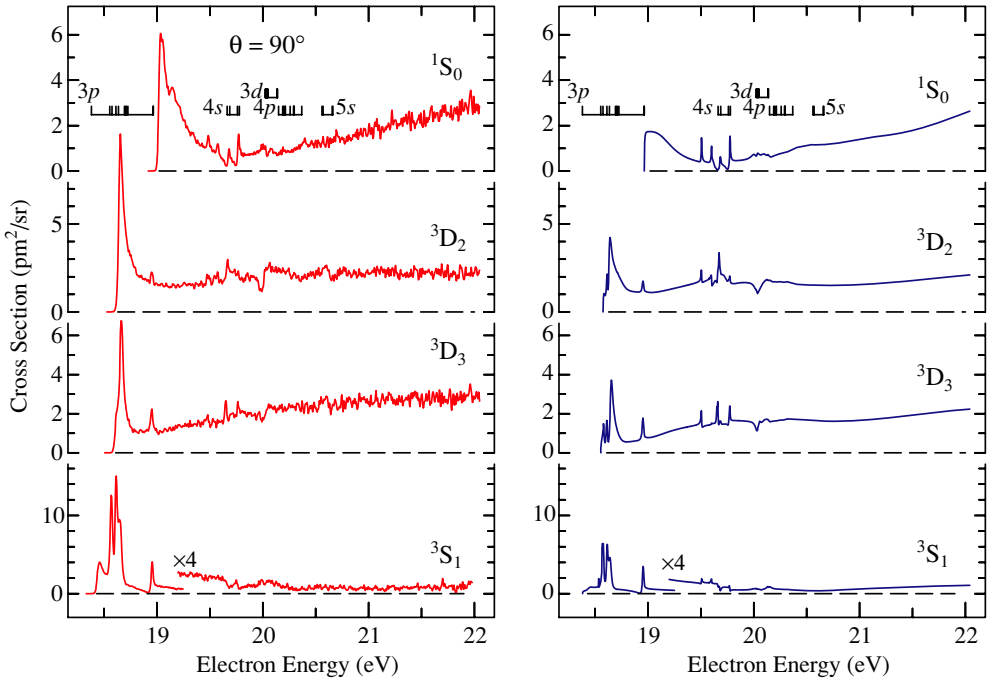


**Figure 11.** As figure 9 at $\theta = 90°$.

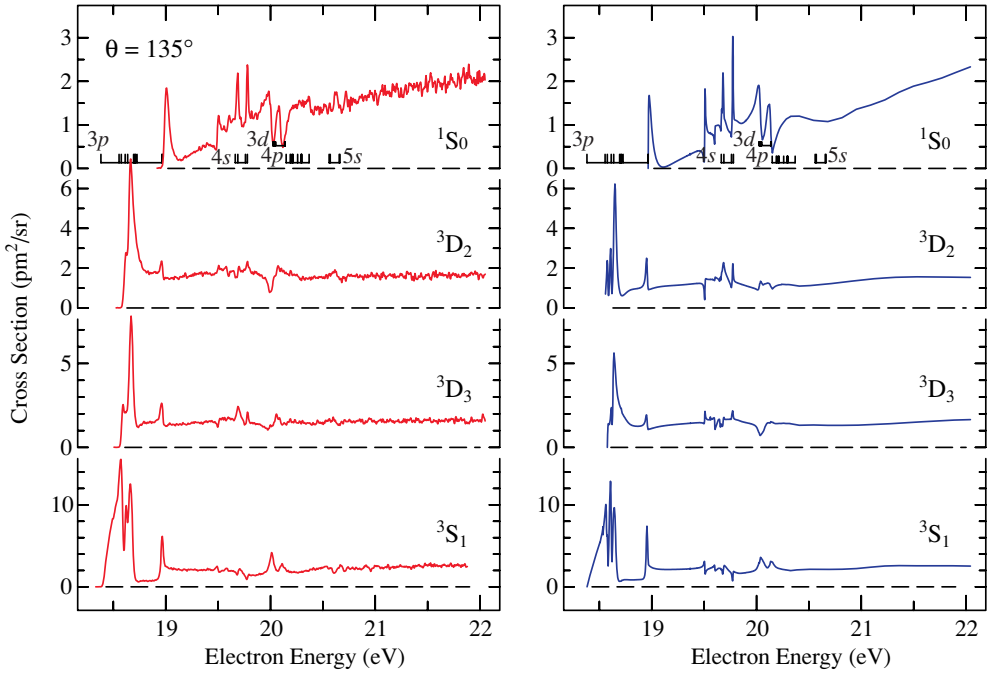


**Figure 12.** As figure 9 at $\theta = 135°$, but without multiplication of the $^3S_1$ results.

the $2p^54p$ and $2p^55s$ target states with excitation energies of about 20.5 eV, the theoretical curves are essentially smooth above 20.2 eV. At several angles, the experimental excitation functions for some members of the $2p^53p$ manifold exhibit structure around 20.5 eV, which is clearly above the noise level and can be associated with higher-lying resonances.

In table 3, we summarize the information deduced from the present data for the positions and widths of resonance feature between 16.9 eV and 20.2 eV incident energy and compare them with the values given by Buckman *et al* [6] (see also table IX in the review of Buckman and Clark [5]). The latter values were deduced from the excitation function for the production of metastable Ne atoms, as measured with about 20 meV resolution and a high signal-to-noise ratio by Buckman *et al* [6]. Also listed for comparison are the results of Bömmels *et al* [7], which were obtained with a high-resolution photoelectron source.

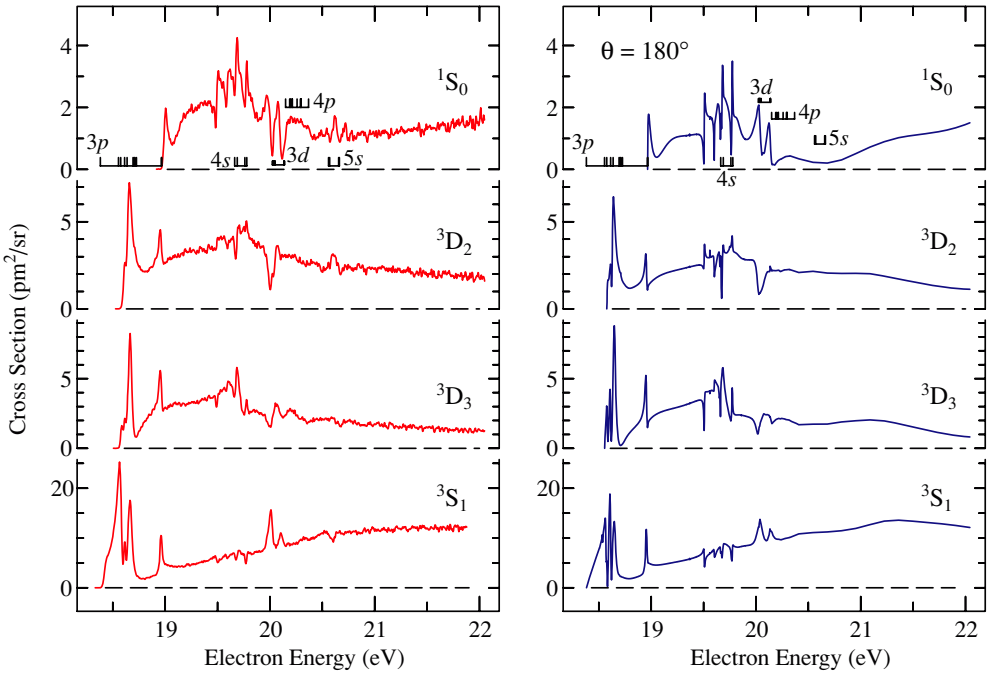


**Figure 13.** As figure 9 at $\theta = 180°$, but without multiplication of the $^3S_1$ results.

**Table 3.** Energies and widths of $Ne^-$ resonance and cusp features in the energy range 16.9–20.2 eV. Only resonances actually observed experimentally in the present work are given—four more resonances in the 18.3–18.55 eV range were listed by Bömmels *et al* [7]. The letters in the second column refer to the notation used by Buckman *et al* [6]. We also list the values derived by Bömmels *et al* [7] for comparison.

| | | Energy (eV) | | | | Width (meV) | | |
|---|---|---|---|---|---|---|---|---|
| Feature | [5] | [7] | Present expt. | Present theory | [5] | [7] | Present expt. | Present theory |
| $2p^5(^2P_{3/2,1/2})3s3p(^3P)$ | 16.906 (10) *b* | 16.903 (3) | 16.904 (10) | 16.901 | 117 | 113 | 97 (15) | 117 |
| $2p^5(^2P_{3/2})3p^2(^1S)$ | 18.580 (10) $d_1$ | 18.573 (3) | 18.576 (10) | 18.570 | 30 | 31 (3) | 26 (8) | 30 |
| $2p^5(^2P_{3/2,1/2})3p^2(^1D)$ | 18.626 (15) *e* | 18.615 (3) | 18.618 (10) | 18.614 | 25 | 18 (4) | 17 (8) | 15 |
| $2p^5(^2P_{1/2})3p^2(^1S)$ | 18.672 (10) $d_2$ | 18.662 (3) | 18.665 (10) | 18.659 | 50 | 42 (3) | 35 (8) | 38 |
| $2p^53p'[1/2]_0 4s$ | 18.965 (10) *p* | 18.957 (3) | 18.957 (10) | 18.953 | 22 | 21 (4) | 24 (8) | 19.4 |
| $2p^54s^2, J = 3/2^-$ | 19.498 (15) $n_1$ | | 19.491 (10) | 19.504 | | | 13 (8) | 10.2 |
| $2p^54s^2, J = 1/2^-$ | 19.598 (15) $n_2$ | | 19.585 (10) | 19.601 | | | 14 (8) | 25.4 |
| $2p^54s[3/2]_1 4p, J = 1/2$ | 19.686 (10) $f_1$ | | 19.683 (10) | 19.684 | 42 | | 16 (8) | 23.8 |
| $2p^54s'[1/2]_1 4p, J = 1/2$ | 19.778 (10) $f_2$ | | 19.772 (10) | 19.772 | 23 | | 15 (8) | 21.1 |
| $2p^54p^2, J = 3/2^-$ | 20.054 (10) $g_1$ | | 20.014 (20) | 20.039 | 60 | | 42 (10) | 56.2 |
| $2p^54p^2, J = 1/2^-$ | 20.150 (10) $g_2$ | | 20.108 (20) | 20.135 | 60 | | 40 (10) | 38.4 |

As a clear reference point, we use the sharp $2p^53p'[1/2]_0 4s$ resonance as the benchmark for the energy calibration. This feature was originally located at 18.965(10) eV by Buckman *et al* and was interpreted as a threshold resonance, associated with the $2p^53p'[1/2]_0$ level, which is spectroscopically located at 18.965 9525 eV [21]. With improved resolution and energy calibration of a laser photoelectron experiment, this resonance was later located experimentally at 18.957(3) eV, in agreement with the theoretical value of 18.956 eV [7]. The present experiment is independently calibrated on the 19.365 eV [25] resonance in helium and yields (to some degree fortuitously) exactly the same value, 18.957(10) eV, albeit with a larger uncertainty reflecting the lower resolution of the present experiment as compared to the laser photoelectron experiment. Note that the current theoretical model yields 18.953 eV, due to the slightly different descriptions of both the target states and the collision problem.

The uncertainty in the position of this resonance thus seems to be less than 10 meV. Both the observed and the calculated resonant profiles are seen to lie below the $^1S_0$ threshold in figure 15 and we thus reiterate the assessment of [7] as a Feshbach resonance below the $2p^53p'[1/2]_0$ threshold, rather than a feature associated with the opening of this excitation channel.

According to theory, the dominant configuration of this Feshbach resonance is $2p^53p'[1/2]_0 4s$ with a predicted decay width of 19.4 meV, in agreement with the experimentally determined width of 21 (4) meV [7]. The width determined in the present experiment (as the square root of the difference between the squares of the width of the observed spectral feature and the instrumental profile of 10 meV) is 24 (8) meV.

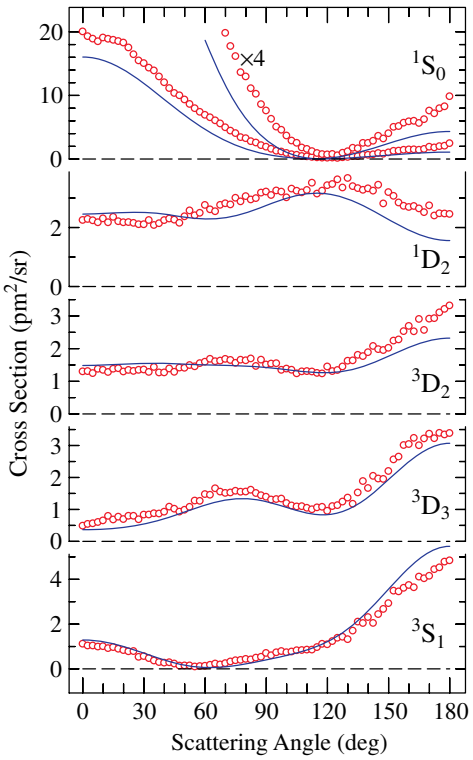


**Figure 14.** Angle-differential cross sections for excitation of the Ne ($2p^5 3p$) states at $E = 19.3$ eV.

This value is compatible with the theoretical and the laser photoelectron values, albeit with a larger uncertainty than the latter experiment.

Figure 15 exhibits an expanded view of the cross sections for the $^1S_0$ state at $\theta = 135°$ and the $^3S_1$ state at $\theta = 180°$. For these situations, the resonance features are particularly pronounced and thus permit a detailed comparison of the observed and calculated resonance profiles. The agreement between theory and experiment is excellent not only in terms of resonance energies and widths, but also in the shapes, i.e., whether they appear as peaks, dips or more complicated Fano profiles. The theoretical energies of the resonances $p - f_2$ agree with experiment to within the accuracy they can be derived with from the experimental data.

The resonances $g_1$ and $g_2$ are, on the other hand, measured about 30 meV lower than calculated. In the $^3S_1$ channel they also appear slightly stronger than calculated, whereas in the $^1S_0$ channel the measured and calculated depths agree. The principal reason for these remaining discrepancies is the omission of some presumably important CI effects. While we classify the $g$ resonances by their dominant configuration $2p^5 4p^2$, it already contains many others in our model. However, our computational resources did not allow us to account for additional mixing with $2p^5 4d^2$, $2p^5 5p^2$, $2p^5 4f^2$, etc. As a result of this omission, the theoretical resonance positions come out slightly too high. Furthermore, the widths are too large, since the positions are too close to the corresponding thresholds.

The effect of the resonance $p$ (at 18.957 eV) on the $^1S_0$ cross section is measured larger than calculated. As already stated above, this could be a consequence of an imperfect correction of the experiment for the instrumental response function. The fact that the measured cross section does not have a vertical onset, in contrast to the calculation, but rises gradually within about the first 30 meV above threshold, is likely of instrumental origin. The efficiency of collecting scattered electrons drops below 30 meV, and this fast drop cannot be reliably corrected for. On the other hand, the fact that

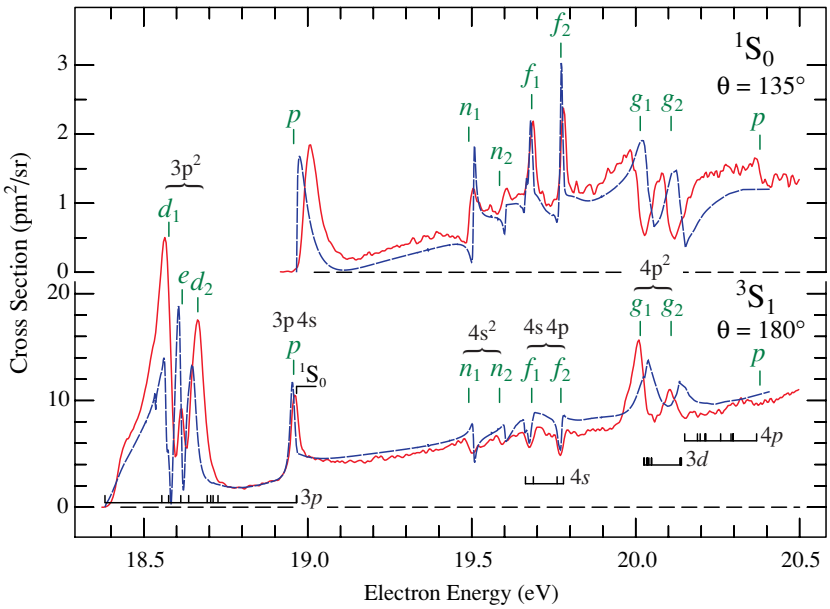


**Figure 15.** Expanded view of the resonant features in selected cross sections for the excitation of the 3p states. Experiment is shown by the more ragged line (red in the online version), theory by the smooth line (blue in the online version). The present experimental energies, labels (using the notation of Buckman *et al* [6], see also table 3), and configurations of the resonances are given above the spectra. Threshold energies are indicated below the lower spectrum.

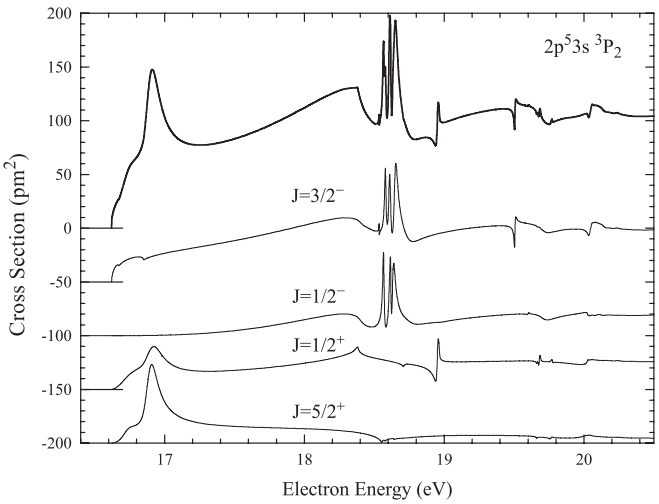


**Figure 16.** Theoretical prediction for the angle-integrated excitation function of the $(2p^5 3s)^2P_2$ state and the most important partial-wave contributions. The latter have been offset on the $y$-scale to improve the readability of the graph.

the height of the feature $e$ in the $^3S_1$ cross section is measured less than the heights of the neighbouring $d_1$ and $d_2$ features, whereas it is calculated as higher, cannot be explained by an imperfect correction for the instrumental response function. Otherwise, this error would apply to all three peaks.

Finally, figure 16 exhibits the theoretical prediction for the angle-integrated excitation function of the $(2p^5 3s)^2P_2$ state and the most important individual partial-wave contributions. As can be seen from the figure, the dominant resonances for this excitation function lie below 19 eV. These were already (re)classified by Bömmels *et al* [7]. Although relatively small in this graph, the resonances in the 19–20 eV incident-energy range are clearly visible as well.

## 5. Conclusions

Substantial progress has been made by both theory and experiment in the ability to accurately determine the cross sections for excitation of neon in the near-threshold regime—particularly interesting for many applications—and even at extreme scattering angles. The *B*-spline *R*-matrix method with non-orthogonal orbital sets has proven to be a powerful tool to predict details of the angle-integrated and the angle-differential electron-impact excitation cross sections of light atoms near threshold—absolute magnitude, overall energy dependence, and the energies and widths of shape and Feshbach resonances.

The agreement of the calculated and the measured values was found to be within 20% for all states and angles studied in the present work and incident energies higher than about 0.3 eV above threshold. The differences are larger within the first 0.3 eV above threshold, but this may well be due to the difficulty of determining the instrumental response function for very slow electrons. Based on the excellent agreement in the predicted features of the excitation functions, it was possible to classify these resonances with an unprecedented accuracy.

## Acknowledgments

This work has been supported by the European Science Foundation (EIPAM Network), by the Swiss National Science Foundation (MA, project no. 200020-113599/1), by the Deutsche Forschungsgemeinschaft (KF and HH) and by the United States National Science Foundation (OZ and KB). KF and HH thank T H Hoffmann for helpful cooperation.

## References

[1] Christophorou L G and Olthoff J K 2000 *Adv. At. Mol. Opt. Phys.* **44** 59
[2] Zatsarinny O and Bartschat K 2004 *J. Phys. B: At. Mol. Opt. Phys.* **37** 2173
[3] Zatsarinny O and Bartschat K 2004 *J. Phys. B: At. Mol. Opt. Phys.* **37** 4693
[4] Zatsarinny O and Bartschat K 2005 *Phys. Rev.* A **71** 022716
[5] Buckman S J and Clark C W 1994 *Rev. Mod. Phys.* **66** 539
[6] Buckman S J, Hammond P, King J C and Read F H 1983 *J. Phys. B: At. Mol. Phys.* **16** 4219
[7] Bömmels J, Franz K, Hoffmann T H, Gopalan A, Zatsarinny O, Bartschat K, Ruf M W and Hotop H 2005 *Phys. Rev.* A **71** 012704
[8] Phillips J M and Wong S F 1981 *Phys. Rev.* A **23** 3324
[9] Allan M 1992 *J. Phys. B: At. Mol. Opt. Phys.* **25** 1559
[10] Stepanovic M, Minic M, Cvejanovic D, Jureta J, Kurepa J, Cvejanovic S, Zatsarinny O and Bartschat K 2006 *J. Phys. B: At. Mol. Opt. Phys.* **39** 1547
[11] Phillips J M 1982 *J. Phys. B: At. Mol. Opt. Phys.* **15** 4259
[12] Register D F, Trajmar S, Steffensen G and Cartwright D C 1989 *Phys. Rev.* A **29** 1793
[13] Khakoo M A 2004 *Phys. Rev.* A **65** 062711
[14] Allan M, Franz K, Hotop H, Zatsarinny O and Bartschat K 2006 *J. Phys. B: At. Mol. Opt. Phys.* **39** L139
[15] Read F H and Channing J M 1996 *Rev. Sci. Instrum.* **67** 2373
[16] Allan M 2000 *J. Phys. B: At. Mol. Opt. Phys.* **33** L215
[17] Allan M 2005 *J. Phys. B: At. Mol. Opt. Phys.* **38** 3655
[18] Nesbet R K 1979 *Phys. Rev.* A **20** 58
[19] Nickel J C, Mott C, Kanik I and McCollum D C 1988 *J. Phys. B: At. Mol. Opt. Phys.* **21** 1867
[20] Zatsarinny O 2006 *Comput. Phys. Commun.* **174** 273
[21] Ralchenko Y *et al* 2008 http://physics.nist.gov/PhysRefData/ASD/index.html
[22] Zatsarinny O and Fischer C F 2002 *J. Phys. B: At. Mol. Opt. Phys.* **35** 4669
[23] Grum-Grzhimailo A N 2003 *Comput. Phys. Commun.* **152** 101
[24] Burke V M and Noble C J 1995 *Comput. Phys. Commun.* **85** 471
[25] Gopalan A, Bömmels J, Götte S, Landwehr A, Franz K, Ruf M W, Hotop H and Bartschat K 2003 *Eur. Phys. J.* D **22** 17